Heliyon 11 (2025) e43303

Contents lists available at ScienceDirect

Heliyon

journal homepage: www.cell.com/heliyon

Research article

Exploring the potential of red muds from Portovesme (SW Sardinia, Italy): Multiscale analysis of REEs content and mineralogy

Emanuela Schingaro [a], Paola Mameli [b,*], Ernesto Mesto [a], Maria Lacalamita [a], Abdelhamid Ouladmansour [a], Giovanna Rizzo [c], Giancarlo Capitani [d], Roberto Conconi [e], Giovanni Mongelli [c]

[a] *Dipartimento di Scienze della Terra e Geoambientali, Università degli Studi di Bari Aldo Moro, Italy*
[b] *Dipartimento di Scienze Chimiche, Fisiche, Matematiche e Naturali, Università di Sassari, Italy*
[c] *Dipartimento di Scienze, Università degli Studi della Basilicata, Italy*
[d] *Dipartimento di Scienze dell'Ambiente e della Terra, Università degli Studi di Milano-Bicocca, Italy*
[e] *UMR 8207-UMET-Unité Matériaux et Transformations Université de Lille, CNRS, INRAE, Centrale Lille, France*

ARTICLE INFO

Keywords:
Red muds
Critical raw materials
Rare earth elements
SEM
TEM
Rietveld analysis

ABSTRACT

Red muds (RMs) from three storage basins at Portovesme (Sardinia, Italy) were investigated combining inductively coupled plasma optical emission spectrometry (ICP-OES), Inductively Coupled Plasma Mass Spectrometry (ICP-MS), X-ray Powder Diffraction (XRPD), Scanning Electron Microscopy (SEM) and Transmission Electron Microscopy (TEM). The oxide composition (wt %), in terms of medians, is as follows: Fe_2O_3 25.63 ± 3.06, Al_2O_3 20.43 ± 2.30, SiO_2 15.65 ± 2.53, Na_2O 8.59 ± 2.48, TiO_2 5.33 ± 1.10, CaO 4.13 ± 0.33. Ba, Ga, Ni, Sr and Zn show significant variation among the trace elements. $\sum$LREEs (292.27 ppm) exhibit greater amount and dispersion with respect to $\sum$HREEs (134.30 ppm). Yttrium (83.50 ± 17.77 ppm) and cerium (231.50 ± 56.80 ppm) were the most abundant among HREEs and LREEs respectively. Quantitative phase analysis (QPA) by Rietveld method indicates the occurrence in the X-ray diffraction patterns of up to 20 different mineral phases out of which the main phases are Fe-oxides, Al-hydroxides, silicates, Ti-oxides, halite and carbonates whereas different combination of minor phases are detected from sample to sample. SEM and TEM investigations show particles with different morphology corresponding to the main phases detected by XRD. SEM also indicates the occurrence of Ba-sulphates, sulphides, Ca-phosphates, as well as HREE-phosphates and Ce-ferrotitanates.

1. Introduction

Red Muds (RMs) or bauxite residues obtained by the Bayer process for alumina production are recognized to be a serious environmental hazard, as they can be disposed in open tailings, dumped in the artificial ponds/dams or dry stacked in open areas. RMs pose worldwide problems due to huge volume of the residue accumulated [1] and to their high alkalinity that makes them a corrosive

---

* Corresponding author.
E-mail address: mamelip@uniss.it (P. Mameli).

https://doi.org/10.1016/j.heliyon.2025.e43303
Received 27 March 2025; Accepted 28 March 2025

material. Efforts for remediation of disposal sites and for the RM reuse as a secondary raw material are steadily increasing [2]. In particular, the intrinsic high alkalinity and significant silica and alumina content can be exploited in the formulations of Alkali Activated Materials (AAMs) with positive effects on setting time, workability, compressive strength, sulphate and fire resistance of the final reaction products [3,4].

In addition, RMs are also considered as a potential polymetallic source, as they are still rich in many valuable metals including rare earth elements (REEs), Sc, and Ga [5]. The last European report on Critical Raw Materials (CRMs) has identified 70 candidates including bauxite/aluminum [6]. Numerous processes have been employed at laboratory, pilot and industrial scale for the CRMs extraction from RMs leached solutions [7–9], thus fostering the transition from a linear to a circular economy. The definition of several features such as physical properties, chemical composition (alumina-to-silica ratio, iron grade, total REEs, etc.) and mineralogy is a fundamental step for the assessment of the appropriate processing route for an efficient CRMs recovery. In this respect, a thorough chemical and mineralogical knowledge on RMs from the Italian storage basins owned by Eurallumina at Portovesme (SW Sardinia) is still lacking. A few and incomplete chemical data were so far published [10–19]. In particular, only one study reports chemical composition including trace elements as determined by ICP (Inductively Coupled Plasma) analyses [12] whereas major and minor elements content from XRF (X-ray Fluorescence) were provided by Mombelli et al. [17,18] and Snars and Gilkes [16]. Other authors, instead, used digestion methods or Scanning Electron Microscopy (SEM) coupled with Energy Dispersive Spectrometry (EDS) to determine the concentration of selected heavy metals [11,13,15,19]. In most of these studies, the potential of RMs from Sardinia as adsorbent material of the heavy metals commonly occurring in contaminated environmental systems [11,13–15,19], as source of iron or other valuable metals [17–19] or as additive in the manufacture of ceramic materials [10] was tested. Budroni et al. [20], instead, evaluated the effects of the mechanical treatment on the mineralogical composition of RMs.

Hematite, gibbsite, boehmite, anatase, sodalite and/or cancrinite and quartz are the mineral phases found in all the previous X-ray diffraction investigations on RMs from Eurallumina. Additionally, goethite and halite [16], bayerite [10], rutile [10,20], andradite [13,15], calcite and thermonatrite [17,18] were also detected. Budroni et al. [20] and Castaldi et al. [13,15] performed Rietveld analysis and found a great variation in the content (wt%) of the crystalline phases and almost 20 wt% of amorphous.

Other known properties of RMs from Eurallumina are: pH 9.75–11.5 [12,13,15,16]; electrical conductivity, EC, 2.1–8.7 mS/cm [13,15]; specific surface area 18.9–31.8 m^2/g [12,13,15,16]; CEC 106.5 $mmol_+/kg$ [13]; total organic matter 0.6 ± 0.07 % [15]; particle size 29 % of <2 μm, 38 % of 2–20 μm, 33 % of >20 μm [16].

In the present study, a multiscale characterization of RMs from Portovesme, Sardinia (Italy) was carried out by combining inductively coupled plasma optical emission spectrometry (ICP-OES), Inductively Coupled Plasma Mass Spectrometry (ICP-MS), X-Ray Powder Diffraction (XRPD), Scanning Electron Microscopy (SEM) and Transmission Electron Microscopy (TEM). To the best of our knowledge, data on REEs and other trace CMs as well as a mineralogical analysis at the nanoscale of RMs from Eurallumina are here reported for the first time. This research is part of an ongoing project aiming to the CMs recovery from RMs based on low cost solid phase extraction methods using novel sorbents and for the reuse of the RMs obtained from the CMs recovery processing in new

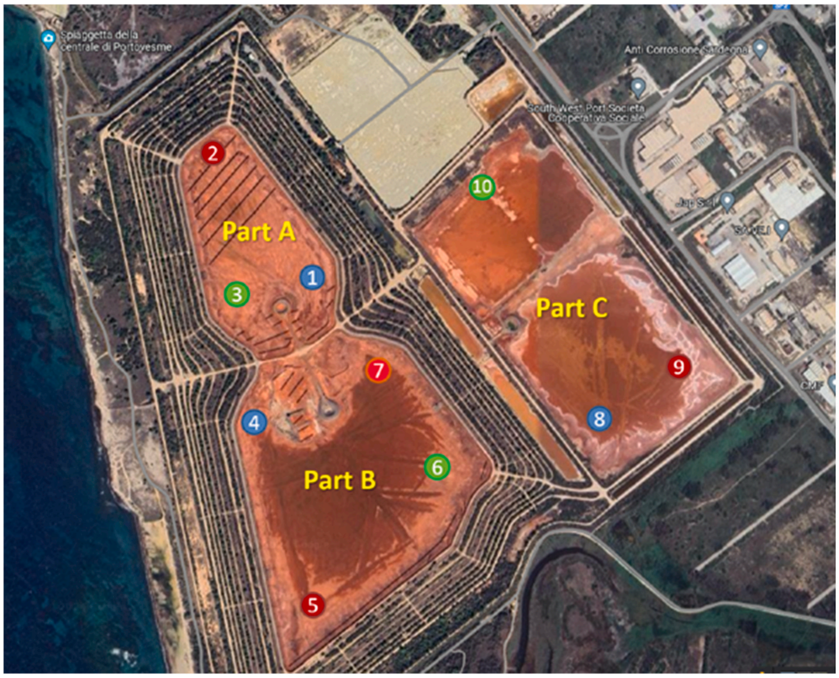

Fig. 1. Satellite image of the Sardinian red muds disposal area (39°10′53″ N 8°24′30″ E), modified after Dentoni et al. [43]. The location of the RMs collecting sites for the studied samples is reported.

formulations of AAMs.

2. Experimental section

2.1. Sample description

The studied RM samples were supplied by Eurallumina company and derive from lateritic (mainly Australian) bauxite ore. Specifically, ten samples (labelled Eur 1 to Eur 10) were randomly collected from three storage basins (hereafter named “Basin A″, “Basin B″ and “Basin C″, Fig. 1) at Portovesme (Sardinia, Italy) in order to obtain an overview of the physico-chemical characteristics of the stored waste. Eurallumina company also provided one sample of the parental bauxite ore (sample labelled Aus). At this disposal site, about 20 Mm^3 of bauxite residues are lagooned on an area of 120 ha and inertized by the sea water [18,21]. The RMs samples were oven-dried at low temperature (65 °C) for 7–10 days and then homogenized using a ZrO_2 ball mill prior to further analyses.

2.2. ICP-MS and ICP-OES

The concentration of Fe, Al, Si, Na, Ti, Ca, Mg, K, P, Mn, Y, Ba, Sc, Sr, V, Zr and Be was measured by inductively coupled plasma optical emission spectrometry (ICP-OES) whereas the remaining trace elements were determined by inductively coupled plasma mass spectrometry (ICP-MS) at Activation Laboratories, Ancaster, Canada. The powdered samples were dissolved by fusion with lithium metaborate/tetraborate, and the resulting molten bead was rapidly digested in a weak nitric acid solution or a multi-acid solution (the latter for Cu, Zn, and Ni). GXR-1, NIST 694, DNC-1, GXR-4, SDC-1, GXR-6, LKSD-3, TDB-1, NOD-P-1, W-2a, DTS-2b, SY-4, CTA-AC-1, BIR-1a, NCS DC86312, ZW-C, NCS DC70009 (GBW07241), OREAS 100a (fusion), OREAS 101a (fusion), OREAS 134a (fusion), and JR-1 standards were used to calibrate the analyses. The analytical uncertainties were within ±5 %, except for elements with concentrations of $\leq$10 ppm, which had uncertainties of 5–10 %.

2.3. XRPD

X-ray powder diffraction patterns were recorded in the 5–80° 2θ range from randomly oriented powder samples. Measurements were carried out in air, at room temperature, using a Panalytical Empyrean X-ray diffractometer with Bragg-Brentano geometry, large beta filter-Nickel detector (PIXcel3D). Experimental conditions were: 1) incident beam, CuKα radiation at 40 kV/40 mA; Soller slits, 0.02 rad; incident beam mask, 15 mm; anti-scatter slit, 1/8°; divergence slit, 1/4°; 2) diffracted beam: anti-scatter slit, 7.5 mm; large β filter; Soller slits, 0.02 rad. Step size 0.0263° and counting time 897.09 s were used. A preliminary qualitative analysis of the diffraction patterns was performed through the PANalytical B.V. HIGHScore Plus software version 3.0e. A quantitative analysis was carried out by the Rietveld method using the Profex (v. 5.3.0) software [22]. Corundum was used as an internal standard (10 % w/w) for the amorphous determination [23]. Background was modelled using a Chebychev polynomial approximation 12th order whereas the peak

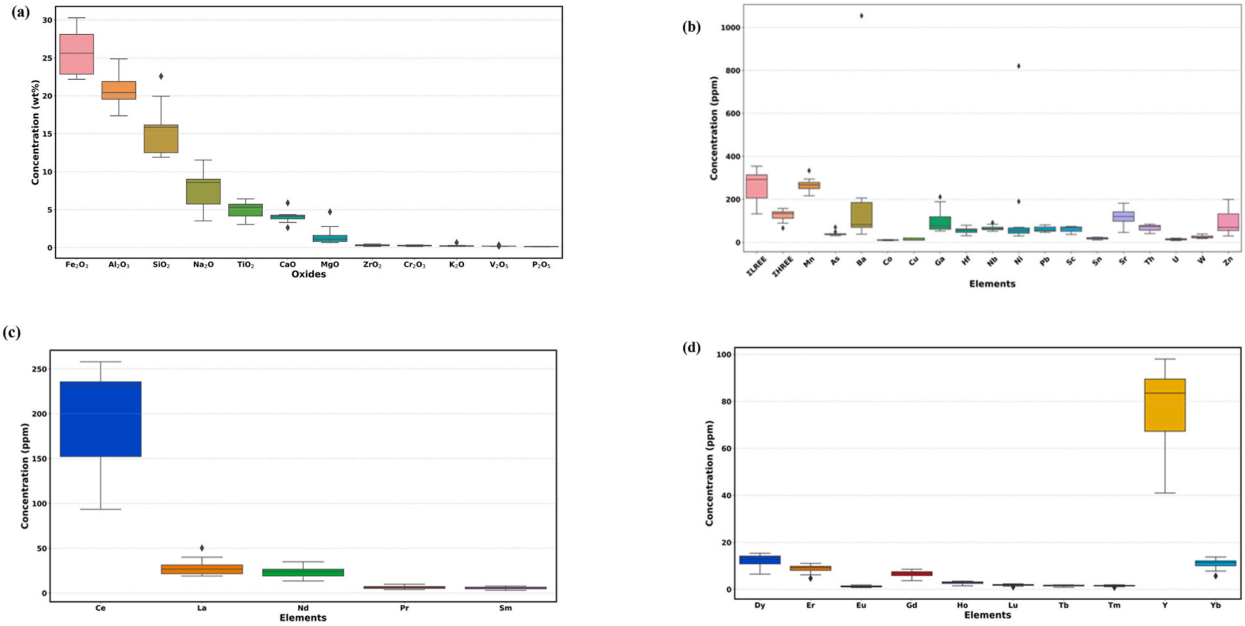

Fig. 2. Box and whiskers plots for (a) major and minor oxides, (b) trace elements, (c) LREEs and (d) HREEs. Ag, Be, Bi, Cs, Ge, In, Mo, Rb, Sb, Ta and Tl which were found below 10 ppm (Table S1) are not shown.

profile was described by a pseudo-Voight function. The scale factor, lattice parameters, particle size, micro-strain and preferential orientation were refined while the atomic coordinates and the isotropic-displacement parameters were kept fixed. The zero shift was also refined.

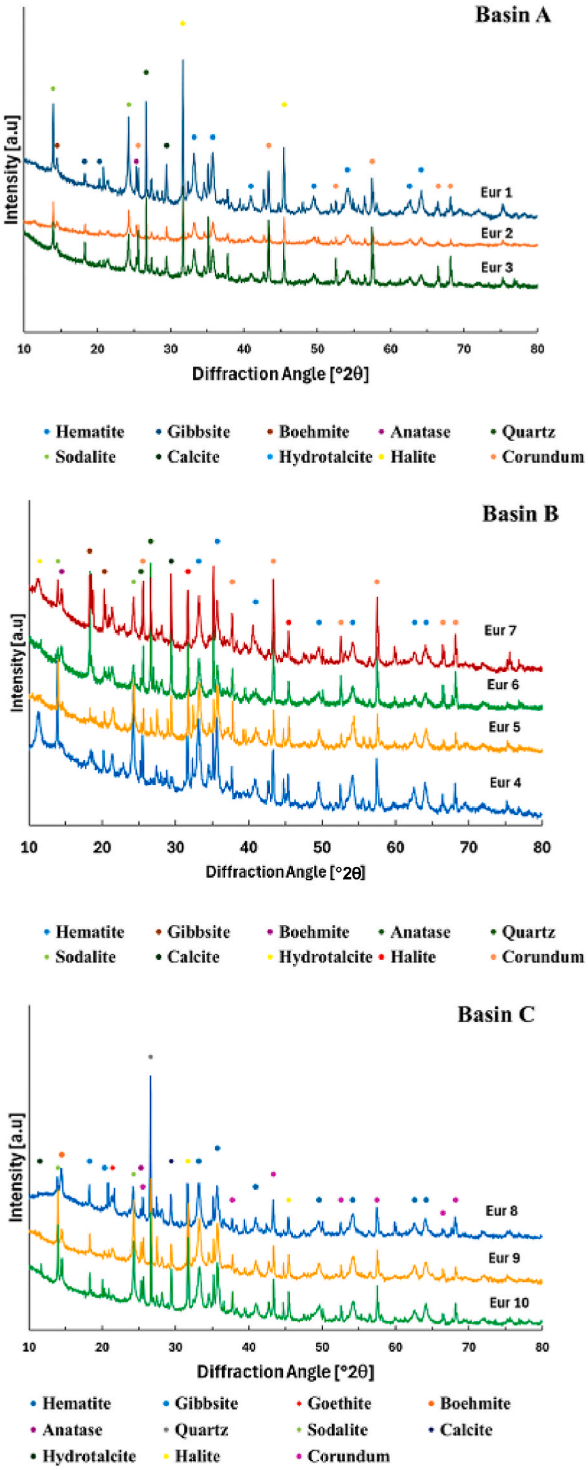

Fig. 3. X-ray diffraction patterns of the studied red mud samples. The expected positions for the identified mineral phases are marked. Corundum was added to the samples as an internal standard.

2.4. SEM and TEM

SEM observations and microanalyses (EDS) were carried out on pellets of samples Eur 3, 6 and 8 after graphite sputter coating (30 nm thick). A ZEISS EVO 50XVP instrument installed at the University of Bari, coupled with EDS (Oxford-Link) and operating at 20 kV and 500 pA was used.

TEM samples were prepared dispersing a small amount of as received “red mud” powder in isopropyl alcohol, followed by ultrasonication for 3 min, then by deposition of few microliters of the dispersion on a carbon film supported by a 300 mesh copper-grid.

TEM investigations were carried out at the Platform of Microscopy of the University of Milano-Bicocca (PMiB) with a JEOL JEM 2100P instrument, equipped with a LaB_6 source, a 9 Mpx Gatan Rio CMOS camera for image acquisition and an 80 mm^2 Oxford Ultimax for EDS analysis. The instrument was operated at 200 keV. Bright Field (BF) and High Resolution (HR) images and Selected Area Electron Diffraction (SAED) patterns were acquired from powder aggregates, as well as EDS maps. For EDS analysis, the instrument was operated in STEM (scanning) mode. Because of the very small grain size of the particles and their close aggregation, EDS mapping revealed more useful than single particle spot analyses, since the latter were always affected by contributions from the surrounding. EDS analyses and maps were acquired with the Aztec software (Oxford) and quantified with the Cliff & Lorimer

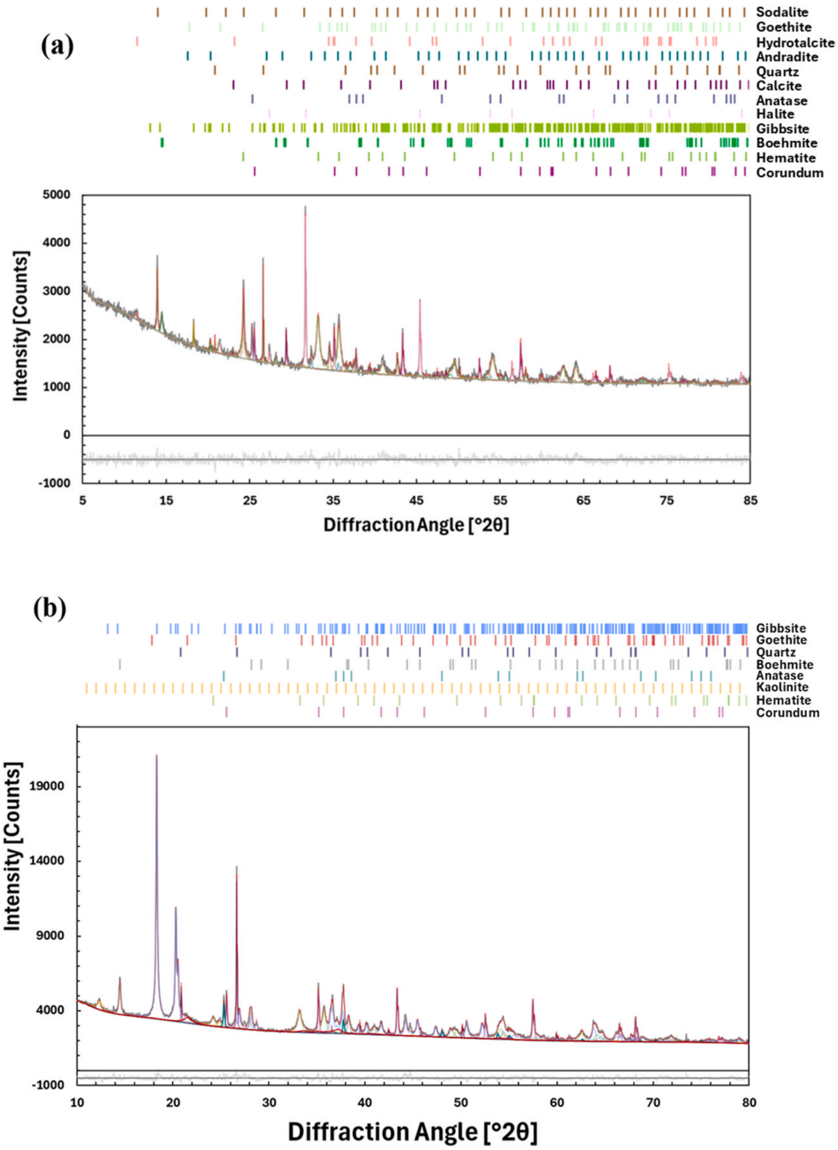

Fig. 4. Results of the Rietveld refinement analysis of the XRD pattern for (**a**) the Eur 2 red mud and (**b**) Aus bauxite. The solid black, red, and gray lines represent the experimental, calculated, and background data, respectively. The vertical bars indicate the expected Bragg reflection positions for the refined mineral phases, with colours matching those of the fitted components. The difference between the experimental and calculated data is shown at the bottom.

approximation [24] using experimental k-factors obtained as described in Conconi et al. [25].

3. Results

3.1. Chemical data

The whole chemical composition of the studied samples is listed in Table S1. Fig. 2, instead, shows the box and whiskers plots for major (>1 wt%) and minor (between 0.1 and 1.0 wt%) oxides as well as for trace elements (<0.1 wt%) including ∑HREEs (Dy, Er, Eu, Gd, Ho, Lu, Tb, Tm, Y, Yb) and ∑LREEs (Ce, La, Nd, Pr, Sm).

The RM major element composition (wt%, in terms of median values) is predominantly characterized by Fe_2O_3 25.63 ± 3.06, followed by Al_2O_3 20.43 ± 2.30 and SiO_2 15.65 ± 2.53, Na_2O 8.59 ± 2.48 and TiO_2 (5.33 ± 1.10).

These elements, along with CaO 4.13 ± 0.33 and MgO 1.09 ± 0.62 exhibit the highest dispersion in content (Fig. 2a). In terms of trace elements (ppm), there is significant variation in Ba (82 ± 59), Ga (76 ± 42), Ni (50 ± 12), Sr (120 ± 42), and Zn (70 ± 19) concentrations (Fig. 2b). The ∑LREEs are more abundant (292.27 ppm) and exhibit greater content dispersion compared to the ∑HREEs (134.30 ppm), Table S1.

Among HREEs, yttrium is the most abundant (83.50 ± 17.77 ppm) whereas among the LREEs abundance of cerium (Ce 231.50 ± 56.80 ppm) is noteworthy (Fig. 2c). In detail, Ce concentration varies between 93.4 and 258 ppm (Table S1).

In Figs. S1 and S2, the chemical composition of the studied RMs is expressed by referring to the sampling sites (Basin A, B and C). Samples from Basin A show the most homogenous composition both in terms of major and minor oxides and trace elements except for the Sr enrichment in Eur 2. In addition, Basin A has the lowest Fe_2O_3 (~23 wt%) and the highest Na_2O (~10 wt%) concentration with respect to the other storage basins. Samples from Basin B evidence remarkable variability mainly in trace elements content. In particular, Eur 4 and Eur 7 samples differ from the other ones for the high amount of Ba, Ga, Sr, Zn and mainly Ni (up to 820 ppm), Fig. S2 and Table S1. Basin B is poorer in SiO_2 (~12 wt%) with respect to Basin A and C (~16 and 20 wt%, respectively). The main feature of Basin C is the relevant concentration in SiO_2 (from 16.07 to 22.59 wt%) and BaO (from 132 to 1054 ppm in Eur 9 and Eur 8 sample, respectively).

Finally, the studied RMs contain trace amounts of radioactive elements such as Th and U as also reported in a recent review on the utilization status of red mud in China [26].

3.2. Mineralogy

The results of XRPD investigation are illustrated in Fig. 3. Rietveld refinements were carried out on all the studied samples. Fig. 4 illustrates the fitting obtained on the Eur 2 (Fig. 4a) and bauxite (Fig. 4b) samples, respectively whereas the quantitative phase analyses are reported in Table 1. The statistical data of refinement parameters are given in Table S2. The Rietveld analysis evidences that the Eurallumina RMs are characterized by a complex mineralogical composition consisting of up to 20 different possible mineral phases (Table 1). In detail, the studied RMs substantially consist of: Fe-oxides/oxyhydroxide (hematite, Fe_2O_3; goethite, $\alpha\text{-}Fe^{3+}O(OH)$; ilmenite, $Fe^{2+}Ti^{4+}O_3$); Al-hydroxides/oxyhydroxide (gibbsite, norstrandite, $Al(OH)_3$; boehmite, $\gamma\text{-}AlO(OH)$; bayerite, γ -$Al(OH)_3$); Ti-oxide (rutile, anatase, TiO_2); silicate phases (quartz, SiO_2; sodalite, $Na_4(Si_3Al_3)O_{12}Cl$; cancrinite, $Na_8(AlSiO_4)_6(CO_3)(H_2O)_2$; andradite, $Ca_3Fe_2Si_3O_{12}$; zircon, $Zr(SiO_4)$); carbonates (calcite, $CaCO_3$; dolomite, $CaMg(CO_3)_2$); layered double hydroxides (hydrotalcite, $Mg_6Al_2(CO_3)(OH)_{16}4H_2O$); halide mineral (halite, NaCl). Hydrogarnet (katoite, $Ca_3Al_2(OH)_{12}$) as well alphaferrite, the latter likely resulting from contamination during the aluminium production were sporadically found. Some of these phases (hematite, goethite, gibbsite, boehmite, rutile/anatase, quartz, sodalite, andradite, calcite and halite) are detected in almost all samples. Most of them are inherited from the parental bauxite that, specifically, contains hematite, goethite, gibbsite, boehmite, anatase, quartz and kaolinite. This is also true for zircon, detected in Eur 3, 6 and 8 samples but not detectable in the bauxite aliquot used for XRPD. The Fe-oxides/oxyhydroxides are the most abundant (from 11.65 to 36.14 wt%) followed by silicates (from 6.25 to 19.37 wt%), Al-hydroxides/oxyhydroxides (about 2.85–15.12 wt%), halite (0.46–8.51 wt%), Ti-oxide (0.33–3.53 wt%) and carbonates (about 0.97–4.63 wt%); only one sample contains substantial hydrotalcite (Eur 4). The concentration of these mineral phases shows the same trend found in the worldwide RMs [7]. The amorphous content of the studied RM ranges from 32 to 49 wt% for all samples, excepting for the Eur 3 and 7. Remarkable variability in the relative phase concentrations is common to all samples. The REE minerals have too low concentration to be detected by XRD but have been identified via SEM (see 3.3. section).

3.3. Electron Microscopy investigations

SEM images show that the studied red muds contain small (less than 50 μm) irregular needles and granular particles as well as aggregated particles (Figs. 5 and 7). Elemental mappings indicate that the red mud is mainly composed of iron, aluminum, titanium, silicon, calcium and sodium. These elements are uniformly distributed in the whole sample whereas chlorine and sulfur appear concentrated in selected areas (Fig. 5). The SEM-EDS spectra indicate the occurrence of several phases including Fe-, Al-, Ti- and Si-oxides, Zr-silicates, NaCl and Ca-sulphates (Fig. 6). However, Ca- and REE-phosphates (Fig. 7a–d), ZnS and Ba-sulphates (Fig. 7b and c) and Ce-ferrotitanates (Fig. 7e) were also identified. In particular, the HREE-phosphates (xenotime, churchite) occur as isolated particles or associated to large grains of Zr-silicates (Fig. 7d). Fig. 7e shows the occurrence of Ce-bearing particles likely ascribable to LREE ferrotitanate species, $(REE,Ca,Na)(Ti,Fe)O_3$, although the EDS spectrum also reveals the contribution of the surrounding matrix particulate.

Table 1
Phase concentration (wt%) of the studied Eurallumina RMs and Australian bauxite.

Phase	Basin A			Basin B				Basin C			
	Eur 1	Eur 2	Eur 3	Eur 4	Eur 5	Eur 6	Eur 7	Eur 8	Eur 9	Eur 10	Aust Bauxite
Hematite	20.0(5)	21.8(8)	12.0(4)	18(1)	18.3(6)	12.6(2)	6.79(18)	15.0(5)	31.0(11)	22.8(6)	9.8(4)
Goethite	0.95(15)	2.7(2)	3.7(3)	4.5(3)	8.6(4)	5.6(3)	4.9(3)	2.5(2)	4.2(5)	0.92(9)	4.4(4)
Ilmenite								1.06(10)	0.90(13)		
Gibbsite	1.35(19)	2.5(3)	1.48(16)	2.7(2)	1.37(16)	7.0(3)	2.14(11)	3.1(3)	2.7(2)	2.53(16)	46(1)
Boehmite	3.1(2)	3.3(3)	1.66(13)	1.8(2)	1.5(2)	6.5(2)	2.53(13)	11.2(9)	4.3(3)	4.5(3)	7.1(4)
Bayerite				2.61(18)			4.90(18)			2.3(2)	
Norstrandite							3.51(18)	0.9(2)		1.0(2)	
Rutile	1.70(17)		0.83(7)	1.06(16)	2.10(15)	2.5(2)		3.3(3)	1.30(12)	0.96(14)	
Anatase	1.33(8)	2.1(3)	1.00(8)	0.74(7)		1.06(9)	0.33(4)	0.19(5)	2.06(17)	1.39(11)	1.99(12)
Quartz	3.81(16)	2.79(13)	1.93(15)		0.55(4)	4.24(17)	4.2(5)	16(4)	3.40(14)	4.95(13)	4.89(10)
Sodalite	8.0(3)	8.5(4)	5.6(2)	6.9(2)	5.3(2)		1.65(8)	2.7(2)	9.5(5)	8.6(3)	
Cancrinite						6.1(2)				2.4(8)	
Andradite	3.5(2)	2.8(3)	2.73(14)	3.8(2)	4.8(2)		0.37(7)		1.32(19)		
Zircon			0.12(3)			0.50(4)		0.44(8)			
Calcite	2.76(16)	2.58(16)	1.76(17)	0.97(11)	2.99(12)	3.80(18)	1.64(12)	3.1(3)	2.4 (3)	2.8(2)	
Dolomite								1.57(14)			
Hydrotalcite		2.5(5)		6.3(9)	2.3(3)	2.0(2)	3.51(18)			0.54(13)	
Halite	8.51(19)	7.9(3)	4.80(13)	2.57(8)	2.84(9)	2.73(7)	1.49(4)	3.04(11)	4.62(19)	0.46(7)	
Katoite						1.29(19)	0.65(11)				
Alphaferrite	0.19(3)			0.49(3)				0.16(3)	0.41(3)	0.38(2)	
Kaolinite											8.8(6)
Amorphous	44(1)	41(2)	62(1)	48(2)	49(1)	44.1(9)	63.8(9)	35(4)	32(3)	43(2)	16(2)

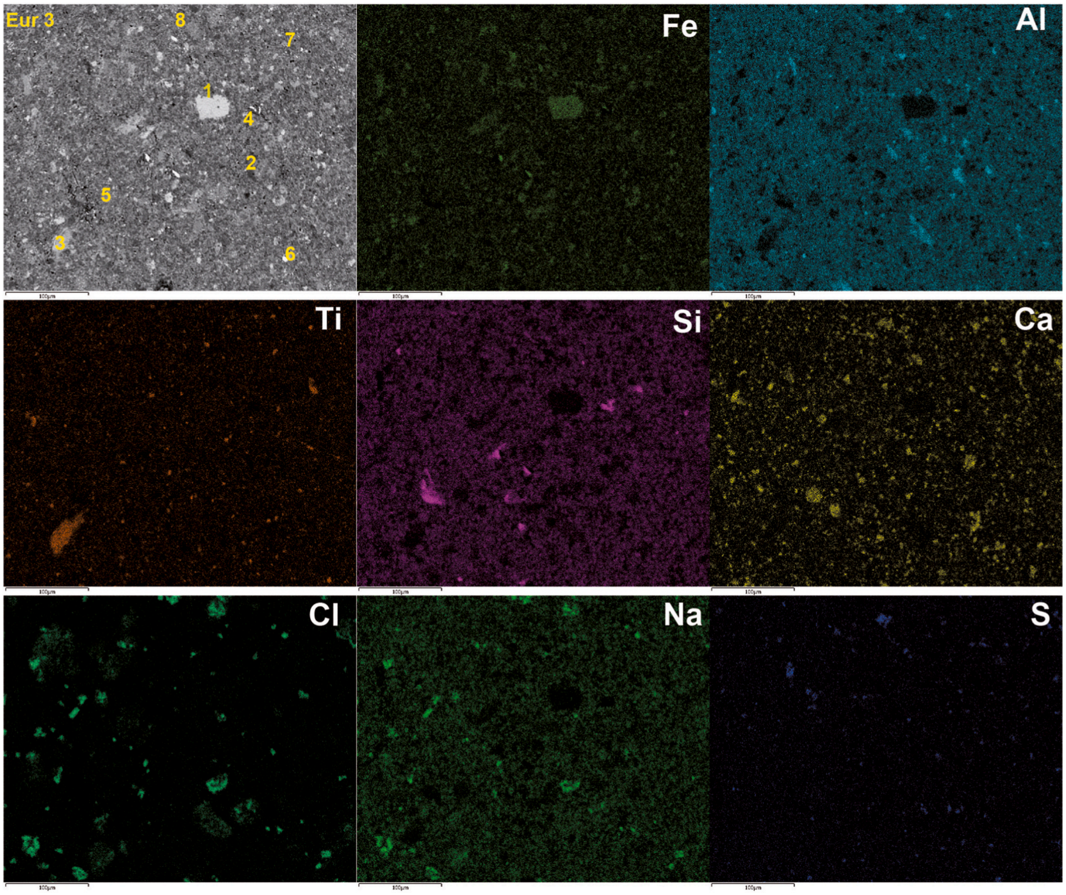

Fig. 5. Backscattered scanning electron image, BSD-SEM and energy dispersive X-ray map of Eur 3 sample. Labels: 1 - Fe-oxide; 2 - Al-oxide; 3 - Ti-oxide; 4 - Si-oxide; 5 - Aluminum silicate; 6 - Zr-silicate; 7 - NaCl; 8 - Ca-sulphate (see also Fig. 6).

TEM images reveal a very broad grain size distribution, from micron-sized to nano-sized crystals and a large variety of morphologies, from acicular to lamellar to irregular forms (Fig.s 8a and c). The polycrystalline SAED patterns acquired on aggregates show sharp diffraction effects aligned along discontinuous rings, testifying the prevailing crystalline nature of the grains. The vast majority of these diffraction effects were indexed as hematite and bohemite (Fig.s 8c and d), although other phases were suggested by peaks unmatching these two phases. Lattice fringe images also show crystallites of different nature and size (Fig. 9a and b). In some cases, lattice fringe spacings are consistent with hematite and boehmite, in some other cases crystals with larger cell parameters are suggested. A deeper understanding of these data would require careful calibration of the TEM camera length and magnification, and correction for lens distortion [27], as the error affecting the measured cell parameters is often greater than the difference between different candidates.

The very small size of the red mud powder and their strong tendency to aggregate did not allow the obtainment of single particle analyses, but EDS mapping allows to identify some element distributions among different grains and phases. EDS maps are reported in Figs. S3 and S4. The average compositions of the mapped area are reported in Table 2. Fe (~42 wt%) and Al (~12 wt%) are the most abundant cations in the analysed red mud powder aggregates, consistently with the detection of hematite and boehmite as major phases, followed by Ti (~3.9 wt%), Si (~3.5 wt%), Na (~1.9 wt%), Mg (~1.8 wt%). As regard the anions, other than O (31 wt%), significant amounts of Cl (1.9 wt%) and S (1.4 wt%) were detected. All other elements are poorly meaningful because very close or below the EDS detection limit (0.3 wt%). Overall, the following relationships among elements were identified: Fe and Al tend to form their own phases, which, according to SAED data should be mostly hematite and boehmite, respectively, but also goethite and gibbsite are possible, according to XRD data; Al, however, is found also correlated with Si and Na, meaning that Al also enters in silicates, as for instance sodalite-cancrinite, according to XRD data. Titanium also forms its own phase (anatase, according to XRPD data), but it is also found correlated with Ca. Other correlations were found between Na and Cl (halite, according to XRD data), Na and S, Ca and P, and Ca and S.

4. Discussion and conclusion

RMs are very complex matrices in terms of crystallinity and number and type of residual and/or neo-formed phases. Feret [28]

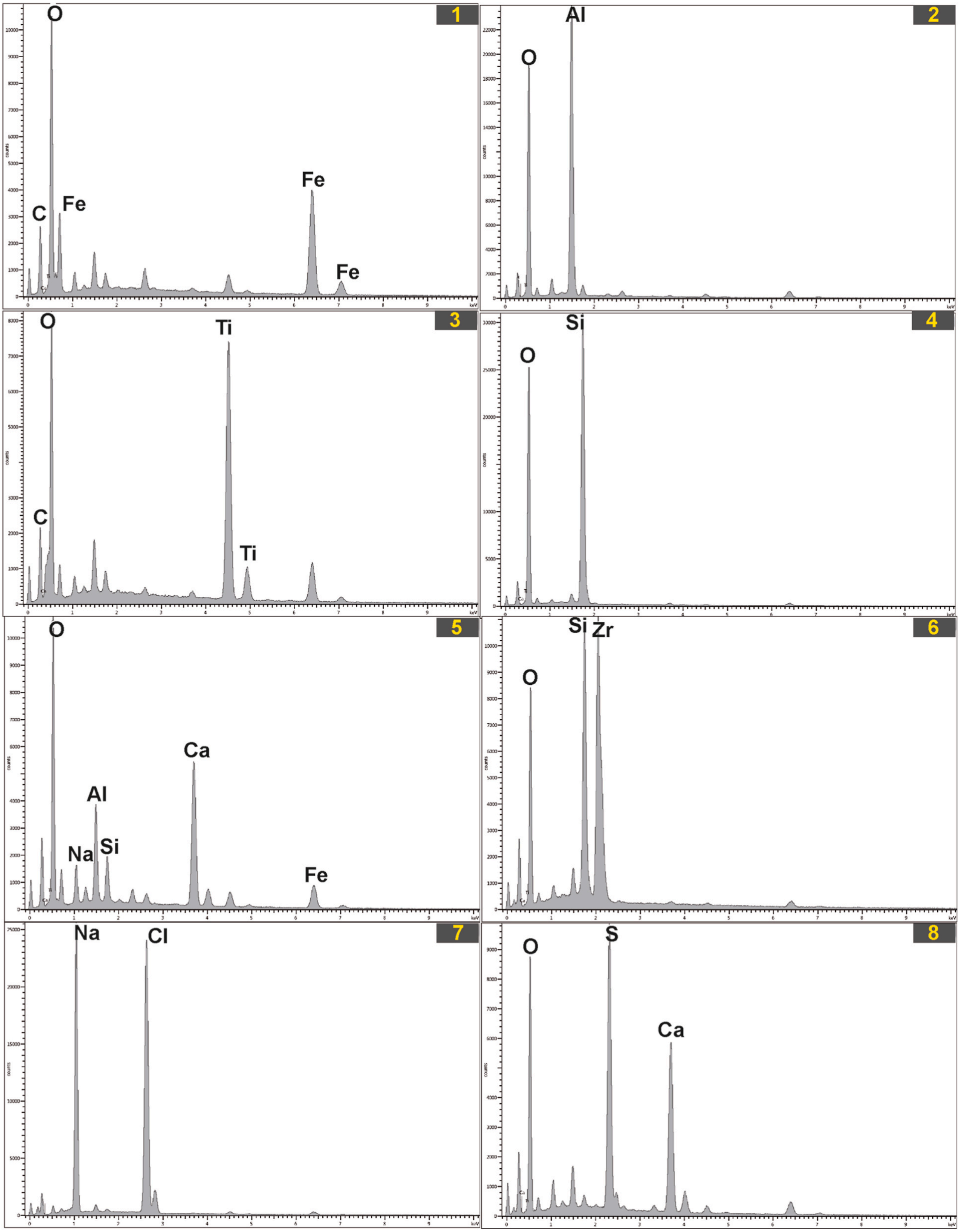

Fig. 6. SEM-EDS spectra associated to the BSD image in Fig. 5. Labels: 1 - Fe-oxide; 2 - Al-oxide; 3 - Ti-oxide; 4 – Si-oxide; 5 – Aluminum silicates; 6 – Zr-silicate; 7 - NaCl; 8 – Ca-sulphate.

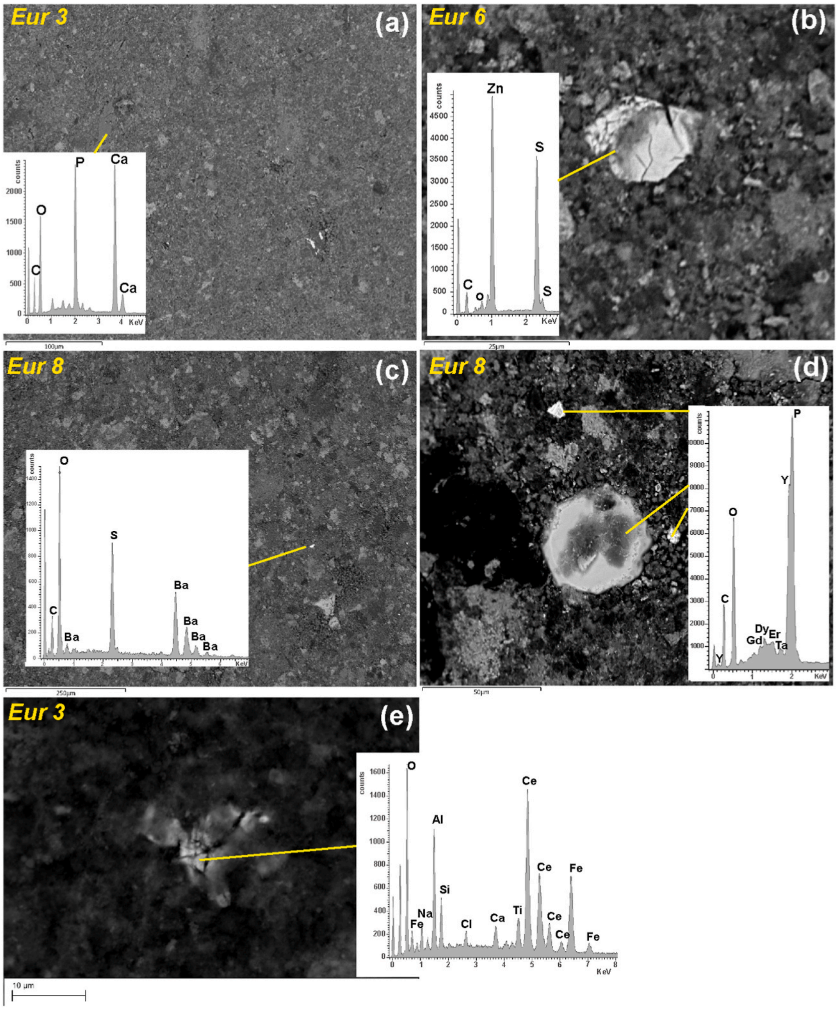

Fig. 7. Backscattered scanning electron image, BSD-SEM of Eur 3, 6 and 8 samples showing selected grains of Ca-phosphate (**a**), ZnS (**b**), Ba-sulphate (**c**), HREE-phosphate (**d**) and Ce-ferrotitanates (**e**). EDS spectra are reported in the inset.

carried out Rietveld refinements starting from a database of 45 possible mineralogical phases detected in RMs and validating the occurrence in the studied samples of up to 28 different minerals. The author observed that the amorphous component in RMs is mainly represented by hydrated sodium aluminium silicates. In addition, limitations in the accurate estimation of the amorphous content with the Rietveld method were found even if synchrotron radiation is used. In the present study the combination the of the Rietveld analysis and of SEM and TEM investigations (see Table 1 and the Results section) provides insights into the phase assemblage so far observed for RMs from Eurallumina. As many as 20 phases have been identified via Rietveld analyses whereas SEM confirmed the occurrence of zircon (sporadically detected via XRPD) and allowed to detect sulphates (anhydrite, gypsum, baryte), sulphides (sphalerite) and phosphates (hydroxyapatite). Notably, also Y-phosphate (xenotime, churchite) and LREE-ferrotitanate species, (LREE,Ca,Na)(Ti,Fe)O_3 are also observed (Fig. 7), thus improving previous knowledge on Eurallumina RMs [13,15–17,20]. Our results are in keeping with recent findings on the occurrence of REE phases in red muds ([29] and references therein; [30]). However, REE speciation in bauxite and bauxite residues can be very complex [31–33] and further investigations are needed on Eurallumina samples for a final assessment on REE's behavior.

The combination of the chemical and mineralogical data allows to draw additional considerations. Indeed, RMs are typically characterized by an order of elemental abundance Fe > Al > Si ~ Ti > Ca > Na [34] whereas in our case the results of the ICP analyses provided Fe > Al > Si > Na > Ti > Ca (Fig. 2, Table S1). The Fe grade of the studied Eurallumina RMs (18.1 wt%) is similar to that found in Snars and Gilkes [16] and Mombelli et al. [17,18], 10.6 and 14.6 wt% respectively. However, higher values (21.30–30.35 wt %) may be derived from data in Sglavo et al. [10], Bertocchi et al. [12] and Castaldi et al. [15]. RMs generated worldwide exhibit Fe grade from ~4.8 wt% (China RMs, [35]) to 39.8 wt% (Worsley Australia RMs, [16]).

The Al/Si ratio varies from 1.33 (this study; [16]) to 1.97 [15] in the Eurallumina RMs. These values are within the overall range (0.72–4.40) found for worldwide RMs [7]. The sodium enrichment of the Eurallumina RMs (7.5–12.06 w% Na_2O) was already detected in previous investigations [10,12,15–18] and was explained with the occurrence of NaCl, presumably due to the RMs washing with sea

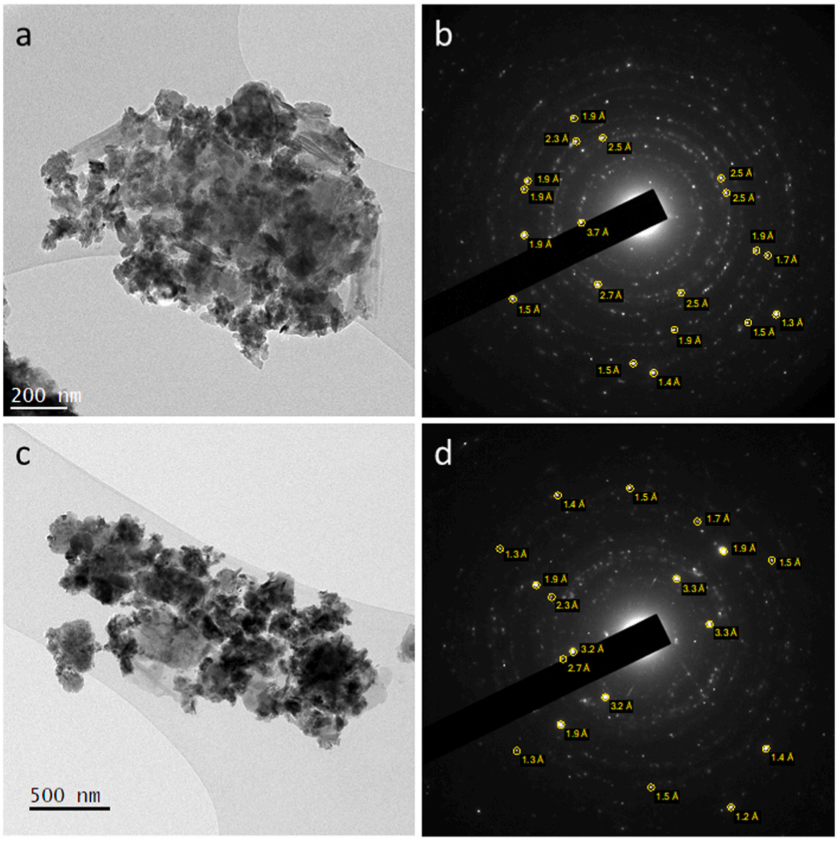

Fig. 8. Representative bright field (BF) TEM images (**a** and **c**) and related selected area diffraction (SAED) patterns (**b** and **d**) of red mud powder. Note the varying dimensions and shapes of grains. In SAED patterns, spacing of planes related to some diffraction spots are indicated, for instance: 3.7 Å is assigned to the $(012)_{HEM}$ planes of hematite (3.68 Å); 2.7 Å to $(104)_{HEM}$ planes (2.70 Å); 2.5 Å to $(110)_{HEM}$ planes (2.52 Å); 1.7 Å to $(116)_{HEM}$ planes (1.70 Å); 1.5 Å to $(214)_{HEM}$ planes (1.49 Å), and so on; 3.2 Å are assigned to the $(021)_{BOH}$ planes of böhmite (3.18 Å); 1.9 Å to $(150)_{BOH}$ planes (1.86 Å).

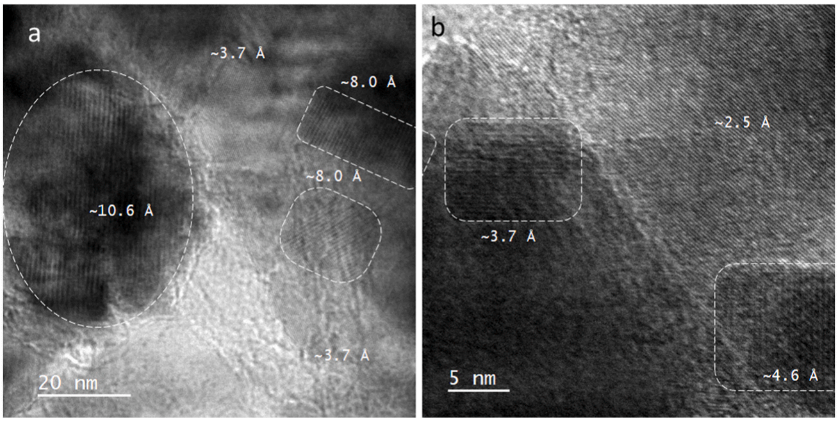

Fig. 9. High resolution images (**a** and **b**) showing lattice fringe with different spacings for different grains. Value at ~3.7 Å in (**a** and **b**) and ~2.5 Å (**b**) can be attributed to hematite $(012)_{HEM}$ and $(110)_{HEM}$ planes, 3.68 Å and 2.52 Å, respectively, but planes with larger spacing belong to other unidentified phases.

water [10]. However, sodium in RMs is mostly in sodalite and subordinately in NaCl, NaOH and/or Na_2CO_3 (Table 1 in the present study; [10]). Actually, in our samples a rather wide variability in the sodium content was found ($3.52 \leq Na_2O \leq 11.54$ w%) with a predominance in RMs from Basin A (Table S1). The calcium content of Eurallumina RMs (from 1.46 wt% in Castaldi et al. [15] to 7.77

Table 2
Average elemental concentration (wt.%) of the areas mapped by TEM-EDS.

wt.%	1	2	3	4	5	6	7	8	9	Mean
O	27.36	26.62	29.84	44.29	25.58	36.30	32.47	30.17	27.67	31.14
Na	1.69	0.00	1.03	0.42	0.87	4.92	5.86	1.51	0.96	1.92
Mg	3.56	3.09	7.27	0.00	0.25	0.32	0.65	0.51	0.45	1.79
Al	6.69	5.50	9.07	44.80	3.18	7.42	10.63	10.95	6.69	11.66
Si	0.87	0.67	0.90	0.60	0.52	17.30	7.90	2.11	0.57	3.49
P	0.00	0.00	0.00	0.00	0.00	0.00	0.00	0.00	0.15	0.02
S	4.79	1.26	1.13	0.00	0.50	2.04	1.54	0.99	0.52	1.42
Cl	0.76	0.00	1.50	0.00	0.27	6.88	6.36	0.37	0.48	1.85
K	0.00	0.00	0.00	0.00	0.14	0.49	0.34	0.22	0.23	0.16
Ca	0.59	0.00	0.00	0.00	0.29	0.51	0.52	0.36	0.35	0.29
Ti	4.62	2.41	3.88	2.04	4.81	2.37	4.04	4.64	5.94	3.86
V	0.00	0.00	0.00	0.00	0.12	0.00	0.00	0.00	0.00	0.01
Cr	0.67	0.00	0.00	0.00	0.29	0.21	0.39	0.43	0.28	0.25
Mn	0.00	0.00	0.00	0.00	0.00	0.00	0.13	0.00	0.12	0.03
Fe	48.41	60.44	45.39	7.86	63.18	21.25	29.18	47.75	55.57	42.11

wt% in Bertocchi et al. [12]) is similar to that found for RMs derived from lateritic bauxites whereas higher values (>10 wt%, [7]) were found for RMs from karst bauxites.

In comparison to the major and minor elements, few data are available in the literature on the content of valuable trace CRMs such as REEs, Sc, Cr, Ga, Ni, V, Zn and Zr in RMs [36,37]. In the case of red muds from Eurallumina, REEs, Sc, Ga and Ni were never measured before. The results of the present investigation provide a total REEs of 0.039 wt%. Agrawal and Dhawan [7] (and references therein) reported LREEs + Y ranging from 0.022 to 0.050 wt% in lateritic RMs from India, Canada and Brazil whereas more variability was observed in karst RMs (from 0.07 to 0.20 wt% for RMs from Greece and China, respectively). In addition, the REEs in our samples were found in the following decreasing order of abundance (median, ppm): Ce (231.5) > Y (83.5) > La (26.80) > Nd (24.1) > Dy (12.9) > Yb (11.5) > Er (9.3) > Gd (6.9) > Pr (6.4) > Sm (6.3) > Ho (3.0) > Lu (1.9) > Tb (1.7) > Tm (1.6) > Eu (1.3). The LREEs (especially Ce, La and Nd) and Y are also the most abundant REEs in both lateritic and karst RMs from around the world [7,38]. Some authors observed that REEs occur as discrete mineral phases or newly formed phases when their concentration is almost 1 wt% (Borra et al., 2015; Vind et al., 2018a). Other authors observed that REEs are involved in isomorphic substitutions of cations with similar radii or are adsorbed on the mineral surfaces [29,39,40].

From moderate to high concentrations, in terms of median values, of scandium (70 ppm), gallium (76 ppm) and nickel (50 ppm) characterize the studied samples. In particular, scandium which is a precious metal with low natural abundance (22 ppm in the Earth's crust), was found associated to hematite, goethite, zircon and titanium bearing phases in the Greek RMs [41] as well as to phosphates in Russian RMs [39]. Mohapatra et al. [42] observed that the amount of Sc, Ni and Cr increases in the order bauxite ore < process sand < red mud whereas the Ga shows an opposite trend; Co, Y, Zr, V, Zn and Nb occur in the highest concentration in process sand.

Finally, the determination of the CRMs concentration in RMs and the definition of the mineral phases where they are hosted, is mandatory for the evaluation of the economic benefit of the CRMs recovery. Ujaczki et al. [37] studied RMs of different origins in terms of maximum recoverable financial value (concentration of CRMs x estimated market price of pure element) of CRMs and elements of high economic importance (REEs, Co, Cr, Ga, In, Ni, Sc, V and Zr). In the studied samples these elements amount to ~4500 ppm which is an intermediate value with respect to the RMs from China (~11000 ppm) and most of RMs around the world [37].

The iron recovery alone from the RMs allows to resume only 15 % of the intrinsic value held by red muds with a possible loss of CRMs and valuable metals. In this regard, more efforts are required to design a process route for the recovery of multiple metals from RMs.

CRediT authorship contribution statement

Emanuela Schingaro: Conceptualization, Data curation, Funding acquisition, Investigation, Methodology, Resources, Supervision, Validation, Visualization, Writing – original draft, Writing – review & editing. **Paola Mameli:** Conceptualization, Data curation, Formal analysis, Funding acquisition, Investigation, Methodology, Resources, Supervision, Validation, Writing – original draft, Writing – review & editing. **Ernesto Mesto:** Data curation, Formal analysis, Investigation, Methodology, Visualization, Writing – original draft. **Maria Lacalamita:** Data curation, Formal analysis, Investigation, Methodology, Validation, Writing – original draft. **Abdelhamid Ouladmansour:** Data curation, Formal analysis, Investigation. **Giovanna Rizzo:** Data curation, Investigation. **Giancarlo Capitani:** Data curation, Formal analysis, Investigation, Methodology, Writing – original draft. **Roberto Conconi:** Data curation, Formal analysis, Investigation, Methodology, Writing – original draft. **Giovanni Mongelli:** Conceptualization, Data curation, Formal analysis, Funding acquisition, Investigation, Methodology, Project administration, Resources, Software, Supervision, Validation, Visualization, Writing – original draft, Writing – review & editing.

Data availability statement

Data will be made available on request. For requesting data, please write to the corresponding author.

Declaration of competing interest

The authors declare that they have no known competing financial interests or personal relationships that could have appeared to influence the work reported in this paper.

Acknowledgments

The study was supported by the project PRIN PNRR 2022 ″Critical Metals in bauxite ore deposits and derived "mining wastes": recovery and reuse for a sustainable future", P.I. G. Mongelli. The Eurallumina company is gratefully acknowledged for providing the samples. XRPD laboratory at the Dipartimento di Scienze della Terra e Geoambientali, University of Bari Aldo Moro, was funded by Potenziamento Strutturale PONa3_00369 "Laboratorio per lo Sviluppo Integrato delle Scienze e delle TEcnologie dei Materiali Avanzati e per dispositivi innovativi (SISTEMA)". Mr. N. Mongelli is acknowledged for the assistance during the SEM analyses at the Dipartimento di Scienze della Terra e Geoambientali, University of Bari Aldo Moro in Bari. Two anonymous reviewers are acknowledged for their insightful suggestions.

Appendix A. Supplementary data

Supplementary data to this article can be found online at https://doi.org/10.1016/j.heliyon.2025.e43303.

References

[1] L. Wang, N. Sun, H. Tang, W. Sun, A review on comprehensive utilization of red mud and prospect analysis, Mineral 9 (6) (2019) 362.
[2] D.R. Zhang, H.R. Chen, Z.Y. Nie, J.L. Xia, E.P. Li, X.L. Fan, L. Zheng, Extraction of Al and rare earths (Ce, Gd, Sc, Y) from red mud by aerobic and anaerobic bi-stage bioleaching, Chem. Eng. J. 401 (2020) 125914.
[3] J. He, Y. Jie, J. Zhang, Y. Yu, G. Zhang, Synthesis and characterization of red mud and rice husk ash-based geopolymer composites, Cement Concr. Compos. 37 (2013) 108–118.
[4] T. Luukkonen, Z. Abdollahnejad, J. Yliniemi, P. Kinnunen, M. Illikainen, One-part alkali-activated materials: a review, Cement Concr. Res. 103 (2018) 21–34.
[5] S. Samal, Utilization of red mud as a source for metal ions-A review, Materials 14 (9) (2021) 2211.
[6] European Commission Study on the Critical Raw Materials for the EU, EIT RawMaterials Call for KAVA Projects SeedBook User Guide, European Union, Brussels, Belgium, 2023, pp. 1–2, 2020.
[7] S. Agrawal, N. Dhawan, Evaluation of red mud as a polymetallic source-A review, Miner. Eng. 171 (2021) 107084.
[8] K. Wang, Z. Dou, Y. Liu, X. Li, G. Lv, T.A. Zhang, Summary of research progress on separation and extraction of valuable metals from Bayer red mud, Environ. Sci. Pollut. Res. 29 (60) (2022) 89834–89852.
[9] X. Pan, H. Wu, Z. Lv, H. Yu, G. Tu, Recovery of valuable metals from red mud: a comprehensive review, Sci. Total Environ. 904 (2023) 166686.
[10] V.M. Sglavo, R. Campostrini, S. Maurina, S. Carturan, M. Monagheddu, G. Budroni, G. Cocco, Bauxite 'red mud' in the ceramic industry. Part 1: thermal behaviour, J. Eur. Ceram. Soc. 20 (3) (2000) 235–244.
[11] C. Brunori, C. Cremisini, P. Massanisso, V. Pinto, L. Torricelli, Reuse of a treated red mud bauxite waste: studies on environmental compatibility, J. Hazard Mater. 117 (1) (2005) 55–63.
[12] A.F. Bertocchi, M. Ghiani, R. Peretti, A. Zucca, Red mud and fly ash for remediation of mine sites contaminated with As, Cd, Cu, Pb and Zn, J. Hazard Mater. 134 (1–3) (2006) 112–119.
[13] P. Castaldi, M. Silvetti, L. Santona, S. Enzo, P. Melis, XRD, FTIR, and thermal analysis of bauxite ore-processing waste (red mud) exchanged with heavy metals, Clays Clay Miner. 56 (4) (2008) 461–469.
[14] P. Castaldi, M. Silvetti, G. Garau, S. Deiana, Influence of the pH on the accumulation of phosphate by red mud (a bauxite ore processing waste), J. Hazard Mater. 182 (1–3) (2010) 266–272.
[15] P. Castaldi, M. Silvetti, S. Enzo, S. Deiana, X-ray diffraction and thermal analysis of bauxite ore-processing waste (red mud) exchanged with arsenate and phosphate, Clays Clay Miner. 59 (2) (2011) 189–199.
[16] K. Snars, R.J. Gilkes, Evaluation of bauxite residues (red muds) of different origins for environmental applications, Appl. Clay Sci. 46 (1) (2009) 13–20.
[17] D. Mombelli, C. Mapelli, C. Di Cecca, S. Barella, A. Gruttadauria, Riduzione di fanghi rossi d'allumina mediante fanghi d'altoforno per la produzione di ghisa, vol. 11, La Metallurgia Italiana, 2016.
[18] D. Mombelli, S. Barella, A. Gruttadauria, C. Mapelli, Iron recovery from bauxite tailings red mud by thermal reduction with blast furnace sludge, Appl. Sci. 9 (22) (2019) 4902.
[19] M. Pietrantonio, S. Pucciarmati, G.N. Torelli, G. D'Aria, F. Forte, D. Fontana, Towards an integrated approach for red mud valorisation: a focus on titanium, Int. J. Environ. Sci. Te. 18 (2) (2021) 455–462.
[20] G. Budroni, G. Cocco, J.Z. Jiang, G. Carturan, S. Enzo, X-ray diffraction and Mössbauer study of red mud residue from alumina production, Mater. Sci. Forum 343 (2000) 695–700.
[21] S. Rai, K.L. Wasewar, D.H. Lataye, J. Mukhopadhyay, C.K. Yoo, Feasibility of red mud neutralization with seawater using Taguchi's methodology, Int. J. Environ. Sci. Te. 10 (2013) 305–314.
[22] N. Doebelin, R. Kleeberg, Profex: a graphical user interface for the Rietveld refinement program BGMN, J. Appl. Crystallogr. 48 (5) (2015) 1573–1580.
[23] T. Westphal, T. Füllmann, H. Pöllmann, Rietveld quantification of amorphous portions with an internal standard-Mathematical consequences of the experimental approach, Powder Diffr. 24 (3) (2009) 239–243.
[24] G. Cliff, G.W. Lorimer, The quantitative analysis of thin specimens, J. Microsc. 103 (2) (1975) 203–207.
[25] R. Conconi, G. Ventruti, F. Nieto, G. Capitani, TEM-EDS microanalysis: comparison among the standardless, Cliff & Lorimer and absorption correction quantification methods, Ultramicroscopy 254 (2023) 113845.
[26] S. Wang, H. Jin, Y. Deng, Y. Xiao, Comprehensive utilization status of red mud in China: a critical review, J. Clean. Prod. 289 (2021) 125136.
[27] G.C. Capitani, P. Oleynikov, S. Hovmöller, M. Mellini, A practical method to detect and correct for lens distortion in the TEM, Ultramicroscopy 106 (2) (2006) 66–74.
[28] F.R. Feret, Selected applications of Rietveld analysis in the aluminium industry, in: C.J. Gilmore, J.A. Kaduk, H. Schenk (Eds.), International Tables for **Crystallography Volume H,** Powder Diffraction, 2019, pp. 782–792.
[29] J. Vind, A. Malfliet, B. Blanpain, P.E. Tsakiridis, A.H. Tkaczyk, V. Vassiliadou, D. Panias, Rare earth element phases in bauxite residue, Mineral 8 (2) (2018) 77.

[30] J. Couturier, P.T. Oularè, B. Collin, C. Lallemand, I. Kieffer, J. Longerey, P. Chaurand, J. Rose, D. Borschneck, B. Angeletti, S. Criquet, R. Podor, H. Pourkhorsandi, G. Arrachart, C. Levard, Yttrium speciation variability in bauxite residues of various origins, ages and storage conditions, J. Hazard Mater. 464 (2024) 132941.

[31] Q. Wang, J. Deng, X. Liu, Q. Zhang, S. Sun, C. Jiang, F. Zhou, Discovery of the REE minerals and its geological significance in the Quyang bauxite deposit, West Guangxi, China, J. Asian Earth Sci. 39 (6) (2010) 701–712.

[32] R.M. Bolanz, S. Kiefer, J. Göttlicher, R. Steinger, Hematite (α-Fe2O3) – a potential Ce4+ carrier in red mud, Sci. Total Environ. 622 (2018) 849–860.

[33] A.M. Borst, M.P. Smith, A.A. Finch, G. Estrade, C. Villanova-de-Benavent, P. Nason, E. Marquis, N.J. Horsburgh, K.M. Goodenogh, C. Xu, J. Kynický, K. Geraki, Adsorption of rare earths elements in regolith-hosted clay deposits, Nat. Commun. 11 (1) (2020) 4386.

[34] S. Wang, H.M. Ang, M.O. Tadé, Novel applications of red mud as coagulant, adsorbent and catalyst for environmentally benign processes, Chemosphere 72 (11) (2008) 1621–1635.

[35] Y. Qu, B. Lian, B. Mo, C. Liu, Bioleaching of heavy metals from red mud using Aspergillus Niger, Hydrometallurgy 136 (2013) 71–77.

[36] Y. Liu, R. Naidu, Hidden values in bauxite residue (red mud): recovery of metals, Waste Manage. (Tucson, Ariz.) 34 (12) (2014) 2662–2673.

[37] É. Ujaczki, V. Feigl, M. Molnár, P. Cusack, T. Curtin, R. Courtney, L. O'Donoghue, P. Davris, C. Hugi, M. Wh Evangelou, E. Balomenos, M. Lenz, Re-using bauxite residues: benefits beyond (critical raw) material recovery, J. Chem. Technol. Biotechnol. 93 (2018) 2498–2510.

[38] C.R. Borra, Y. Pontikes, K. Binnemans, T. Van Gerven, Leaching of rare earths from bauxite residue (red mud), Miner. Eng. 76 (2015) 20–27.

[39] J. Vind, A. Malfliet, C. Bonomi, P. Paiste, I.E. Sajo, B. Blanpain, A.H. Tkaczyk, V. Vassiliadou, D. Panias, Modes of occurrence of scandium in Greek bauxite and bauxite residue, Miner. Eng. 123 (2018) 35–48.

[40] S. Abhilash, M.K. Sinha, B.D. Pandey, Extraction of lanthanum and cerium from Indian red mud, Int. J. Miner. Process. 127 (2014) 70–73.

[41] R.M. Rivera, G. Ounoughene, C.R. Borra, K. Binnemans, T. Van Gerven, Neutralisation of bauxite residue by carbon dioxide prior to acidic leaching for metal recovery, Miner. Eng. 112 (2017) 92–102.

[42] B.K. Mohapatra, B.K. Mishra, C.R. Mishra, Studies on metal flow from khondalite to bauxite to alumina and rejects from an alumina refinery, India, in: C. E. Suarez (Ed.), Light Metals 2012, Springer, Cham, Switzerland, 2012, pp. 87–91.

[43] V. Dentoni, B. Grosso, F. Pinna, Experimental evaluation of PM emission from red mud basins exposed to wind erosion, Mineral 11 (4) (2021) 405.